Microscopic description of 295 MeV polarized protons incident on Sn isotopes

W. Haider,[1] Manjari Sharma,[1] Y. K. Gambhir,[2] and S. Kailas[3]

[1]*Department of Physics, AMU, Aligarh, India*
[2]*Department of Physics, IIT, Mumbai, India*
[3]*Nuclear Physics Division, Bhabha Atomic Research Centre, Mumbai, India*

We present a Brueckner theory analysis of proton-scattering data from Sn isotopes at 295 MeV. A soft-core Urbana v_{14} internucleon potential has been used to calculate reaction matrices that are folded with point-nucleon (both proton and neutron) densities obtained in the relativistic mean field (RMF) framework to calculate the optical potential. We get reasonably satisfactory agreement with the differential cross-section and analyzing-power data using only three scaling parameters for all isotopes. It is observed that the calculated neutron skin increases smoothly as the neutron number increases, in conformity with earlier findings.

I. INTRODUCTION

The scattering of intermediate-energy protons provides an excellent means of extracting information about certain aspects of nuclear structure as well as the two-nucleon interaction inside nuclear matter. The dependence of scattering observables on neutron- and proton-density distributions in nuclei is expected to provide information that may be compared with results using other probes and also with nuclear structure calculations. The relative transparency of the nucleus at intermediate energies increases the sensitivity of the models used and, in particular, to the components depending on spin. It has been observed that the differential cross-section data show greater sensitivity to the spin-orbit potential at intermediate energies [1]. Thus, the intermediate-energy nucleon scattering can be used as a test of the effective nucleon-nucleon interaction and the density distribution of nucleons.

Electron scattering has proven to be helpful in obtaining reliable charge distributions and thus proton densities in nuclei. It has been shown [2,3] that the neutron skin is closely related to the symmetry term of the equation of state. Thus, the determination of the neutron-density distribution has become increasingly important. Karataglidis *et al.* [4], using a reaction-matrix approach, have shown that the proton differential cross section is sensitive to the assumed neutron distribution in target nuclei. In view of this, Amos *et al.* have studied [5] the proton- and neutron-matter distribution in tin isotopes in an extensive analysis of proton-scattering data up to 200 MeV using matter densities obtained from the spherical mean field Hartree-Fock-Bogoliubov (HFB) model with Skyrme-type interactions.

Dirac phenomenology [6,7], involving several parameters, has proven to be quite successful in explaining proton-scattering data—especially spin observables—in the intermediate-energy region. Huthcheon *et al.* [8] analyzed the 200- to 500-MeV proton-scattering data from ^{40}Ca and ^{208}Pb using two phenomenological and two microscopic models. They found that the reaction matrix approach [9] gives agreement only in the extreme forward angles and overestimates the differential cross sections at intermediate angles. They conclude that it is perhaps due to inadequate treatment of self-consistency in obtaining the reaction matrices. Furthermore, their results indicate that even at these energies the scattering observables are sensitive to only the surface region of the potentials used. Kaki and Toki [10] successfully analyzed the 200- to 400-MeV proton elastic scattering data from ^{58}Ni and ^{120}Sn by using the relativistic impulse approach [10–12] and RMF densities with the TMA parameter set [13].

Recently Terashima *et al.* [14] have measured differential cross-section and analyzing-power data for the scattering of 295-MeV protons from five tin isotopes with an aim of studying systematic changes in neutron distribution. They were able to obtain satisfactory agreement with the data using the relativistic impulse approximation [11]. However, as a first step they rescaled [14,15] masses and coupling constants of some of the mesons to fit the proton-scattering data from ^{58}Ni at 295 MeV, assuming the same neutron- and proton-density distribution in this target. This rescaling is identified as the medium effect [14–16]. By using these rescaled interactions, they parameterized the neutron distribution in tin isotopes as a sum of twelve Gaussians for each target. The parameters of the Gaussians were adjusted to obtain agreement with the proton differential-scattering and analyzing-power data at 295 MeV. The neutron skin thus obtained is in satisfactory agreement with results obtained from other sources (see Fig. 12 in Ref. [14]).

In this article we present an analysis of this new data [14] for tin isotopes ($^{116-124}$Sn) at 295 MeV using first order Brueckner theory with a soft-core Urbana v_{14} internucleon potential. The required nucleon density distributions are obtained in the relativistic mean field (RMF) approach [17–19]. The RMF theory is now known to give an exceptionally good account of the ground-state properties of nuclei spread over the entire periodic table. Here, the relativistic Hatree-Bogoliubov (RHB) equations [17–19] are solved in the spherical oscillator basis employing the NL3 [20] Lagrangian parameter set along with the Gogny D1S interaction [21,22] in the pairing channel.

In view of the failure of the earlier reaction matrix approach [9] and the importance of relativity [10] at intermediate energies, we use relativistic kinematics for calculating the reaction matrices. Furthermore, we have made a careful

calculation of the spin-orbit potential avoiding the short range approximation [23,24] for the dominant direct part of the spin-orbit potential. Thus, the present approach differs from the one used in Refs. [23–25] in two important respects: First, we use relativistic kinematics, which necessitates a recalculation of the self-consistent nucleon-matter optical potential and, to see their effect on observables, we compare our results with those obtained by using nonrelativistic kinematics. Second, the folding integral for the direct part of the spin-orbit potential has been calculated exactly, and we show that the effect of approximation used by Brieva and Rook (to be denoted as BR) [26] on the calculated spin-orbit potential is non-negligible. Furthermore, we note that the approximation affects the cross-section and analyzing-power data, even at intermediate angles. For the exchange parts we use the equivalent local approximation [23,24,26]. A similar approximation has also been used in Ref. [8] and for p-^{40}Ca [25] at 200 MeV. We are able to obtain satisfactory agreement with the data using only three scaling parameters for all five isotopes of tin.

Recently [27], we have used our approach for analyzing the 65-MeV proton- and neutron-scattering, reaction, and total cross-section data over a wide mass region: ^{12}C – ^{208}Pb. The agreement with the data is satisfactory.

The method of calculating the optical potential is described briefly in Sec. II. Our results for the proton differential cross-section and analyzing-power data from $^{116, 118, 120, 122, 124}$Sn are discussed in Sec. III. In the same section, we also show that the predictions of our model give fairly good agreement with proton total-reaction cross-section data at two energies from all even isotopes of tin (for which the data is available). Section IV gives our conclusions.

II. METHOD OF CALCULATION

In order to calculate the microscopic optical potential in Brueckner theory, one requires only two inputs; namely, the basic nucleon-nucleon interaction to calculate the reaction matrices and point-nucleon densities to be used for folding.

We solve the Bethe-Goldstone integral equation to obtain reaction matrices using the soft-core Urbana v_{14} [28] internucleon potential, as in Refs. [23–25], with the difference that we use relativistic kinematics for calculating the momenta of both the incident and target nucleons. Furthermore, we use relativistic kinematics for calculating the energies with a continuous choice for intermediate states. Self-consistency is achieved in about five cycles for each of the 17 nuclear matter densities spread evenly over the range 0.6–2.0 fm^{-1} of Fermi momentum k$_F$, in the incident momentum region 0.0–8.0 fm^{-1}. In order to obtain the proton-nucleus optical potential, we fold the appropriate reaction matrices (as defined in Ref. [24]) over the proton- and neutron-matter densities obtained with in the RMF framework [17,19].

In view of the importance of spin at intermediate energies, we avoid the normally used short-range approximation and calculate the folding integral for the direct part without any approximation, as described bellow. Furthermore, Hutcheon [8] also finds that the empirical spin-orbit potential required at

these energies is smaller than that calculated microscopically [9]. The direct part $V_{SO}^{D,p}(r_1, E)$ of the proton-nucleus spin-orbit potential in the folding model approach [23,24,26] as obtained by BR [26] is

$$
V_{SO}^{D,p}(r_1, E) = -\frac{1}{2r_1} \left[\int \rho_p(|\vec{r}_1 + \vec{x}|) g_{SO}^{D,pp} \, x \cos(\theta) \, d\vec{x} \right.
$$
$$
\left. + \int \rho_n(|\vec{r}_1 + \vec{x}|) g_{SO}^{D,pn} \, x \cos(\theta) d\vec{x} \right] \vec{l}_1 . \vec{s}_1, \quad (1)
$$

where $g_{SO}^{D,pp}$ and $g_{SO}^{D,pn}$ are the direct parts of the proton-proton and proton-neutron effective interaction (reaction matrices), ρ_p and ρ_n are the proton and neutron densities in the target, and $\vec{l}_1$ and $\vec{s}_1$ are the orbital and spin angular momentum of the incident nucleon.

After obtaining Eq. (1), BR makes an expansion of ρ around x = 0, assuming the short-range nature of the effective spin-orbit reaction matrix by retaining only first-order terms in the derivative of the density. Thus, BR uses only the lowest order term of an infinite series. However, we calculate the integral numerically in Eq. (1) without making any approximation. The differences between our results and those using the BR approximation are discussed in Sec. III. We find that these differences have substantial effects on both differential cross-section and analyzing-power data at 295 MeV.

The exchange part of the spin-orbit interaction is calculated as in refs. [23,24,26].

The required nucleon-density distributions are obtained in the RMF approach [17]. We solve the RHB equations [17–19] in the spherical oscillator basis employing NL3 [20]; the most successful Lagrangian parameter set along with the Gogny D1S interaction [21,22] in the pairing channel. The calculations reproduce the experiment rather well, as expected. The calculated RHB density distributions both for protons and neutrons resemble closely the corresponding HFB distributions with Skyrme-type interactions, as reported by Amos *et al.* [5]. The neutron skin predicted by the RHB densities used here are slightly higher compared with those of Refs. [5,14]. These RHB densities for tin isotopes have recently been used [29] in a reaction-matrix approach to predict the weakening of proton-nucleus spin-orbit interaction with the addition of neutrons. By using these RHB densities and the reaction matrices, we calculate the optical potential [$V(E, r)$, $W(E, r)$, $V_{SO}(E, r)$, and $W_{SO}(E, r)$] using the folding procedure [23,24] for all five tin isotopes at 295 MeV. In order to obtain agreement with the experimental data we multiply each component of the calculated potential by scaling parameters λ. The potential used by us in a spherical optical model code is

$$
U(E, r) = \lambda_R V(E, r) + i\lambda_I W(E, r) + \lambda_{SO}^R V_{SO}(E, r)
$$
$$
+ i\lambda_{SO}^I W_{SO}(E, r). \quad (2)
$$

Thus, we have four adjustable parameters (λ_R, λ_I, λ_{SO}^R, and λ_{SO}^I) to obtain the best fit to the data by minimizing χ^2/DF (where DF stands for degrees of freedom).
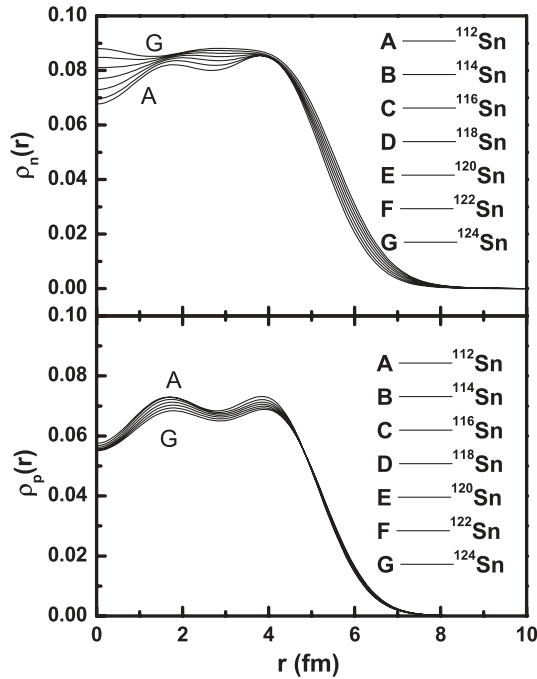
FIG. 1. The neutron and proton distribution in tin isotopes as obtained by our RMF calculations.

III. RESULTS AND DISCUSSION

The calculated neutron and proton densities are shown in Fig. 1. Our results show that the RHB density distributions both for protons and neutrons resemble closely the corresponding HFB distributions with Skyrme-type interactions as reported by Amos *et al.* [5]. Notice that, as we add more neutrons (going from ^{112}Sn to ^{124}Sn), the shape of the proton-density distribution remains almost unchanged, whereas the depression at the center changes to a hump in the neutron distribution because of shell filling, which is consistent with the results of Ref. [5].

The rms charge radius, shown in Fig. 2(a) and which increases with neutron excess, is in close agreement with electron scattering [30], muonic x-ray data [31], and the combined results of electron scattering and muonic x-ray data [32].

The rms radii of both the proton and neutron densities slowly increase with the addition of neutrons. The neutron skin [shown in Fig. 2(b)] increases with neutron excess from 0.115 fm for ^{112}Sn to 0.280 fm for ^{124}Sn; a value slightly higher than those found in Ref. [14]. Figure 2(b) shows that our RMF results for neutron thicknesses, although higher, are still within the uncertainties of results from 800-MeV proton scattering [33], giant-dipole resonance [34], spin-dipole resonance [35], antiprotonic x-ray data [36], and results from Terashima *et al.* [14]. Thus, various probes are able to give a range of skin thicknesses consistent with the data [37].

By using the method described in Sec. II, we have calculated the optical potential for the scattering of protons from tin isotopes.

In Fig. 3, we show the calculated direct and exchange parts of the real central [Fig. 3(a)] and the spin-orbit part [Fig. 3(b)] of the optical potential for p-^{120}Sn at 295 MeV. We
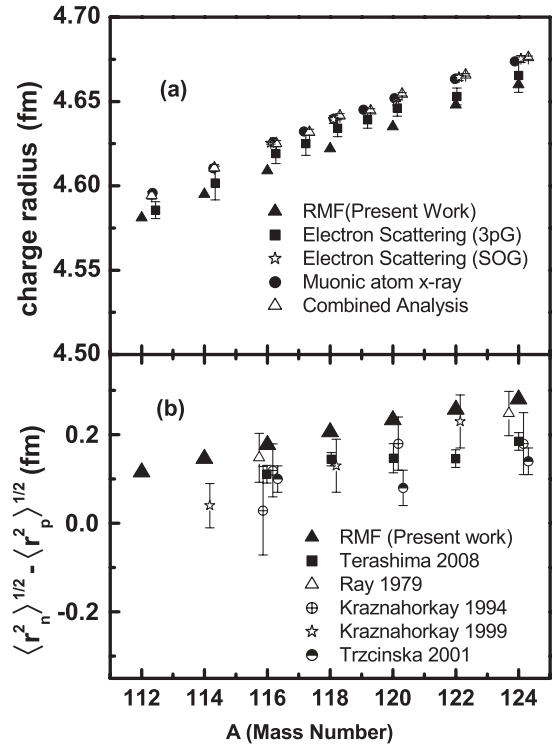

FIG. 2. (a) Existing experimental data on rms charge radii of the tin isotopes along with the present RMF results (solid triangles). Solid squares, solid stars, solid circles, and open triangles are respectively the results from electron scattering using different shapes of the charge distribution [30], muonic atom x-ray [31], and combined electron scattering and muonic x-ray data [32]. (b) Neutron skin thicknesses. Solid triangles are the results from present work (RMF). Solid squares, open triangles, crossed circles, stars, and shaded circles are respectively the results from Terashima *et al.* [14], 800-MeV proton scattering [33], giant dipole resonances [34], spin-dipole resonances [35], and anti-protonic x-ray data [36].

note that the exchange part at this energy is quite small, and thus the equivalent local approximation would not cause a big error. Figure 3(b) shows our results (denoted as NEW) for the calculated real spin-orbit potential using Eq. (1) and the BR approximation (denoted as OLD) (Eq. (9) of Ref. [26]). We find that, besides reducing the strength near the origin, the use of Eq. (1) leads to non-negligible changes around the peak value.

The calculated optical potential is used in a spherical optical model code to calculate the differential cross-section and analyzing-power data for the scattering of 295-MeV protons from $^{116, 118, 120, 122, 124}$Sn. The λ scaling parameters are adjusted to minimize χ^2/DF. A value of $\lambda < 1$ (>1) implies that the calculated potential is larger (smaller) than that required by the data.

We find that we are able to get good agreement with the differential cross-section (Fig. 4) and a reasonable agreement with the analyzing-power data (Fig. 5) for all isotopes $^{116, 118, 120, 122, 124}$Sn using only three scaling parameters in comparison with twelve Gaussians for each target [14]. Our values are: $\lambda_R = 0.722$, $\lambda_I = 0.760$, and $\lambda_{SO}^R = 0.831$,

TABLE I. Calculated reaction cross section σ_R^{theo}(mb) for 22.8- and 65.5-MeV protons compared with experimental reaction cross sections σ_R^{Exp}(mb).

Target	$E_p = 22.8$ MeV		$E_p = 65.5$ MeV	
	σ_R^{theo}(mb)	σ_R^{exp}(mb) Ref. [38]	σ_R^{theo}(mb)	σ_R^{exp}(mb) Ref. [39]
^{112}Sn	1447.5	1430 ± 61	1497.9	1411.4 ± 43.1
^{114}Sn	1480.6	1461 ± 62	1528.0	–
^{116}Sn	1515.2	1530 ± 45	1557.8	1502.6 ± 44.1
^{118}Sn	1548.5	1559 ± 52	1586.6	1535.6 ± 47.3
^{120}Sn	1566.8	1589 ± 38	1613.7	1513.2 ± 44.5
^{122}Sn	1603.5	1595 ± 59	1638.9	–
^{124}Sn	1625.2	1583 ± 55	1662.4	1623.3 ± 55.0
^{208}Pb	1610.7	–	2143.3	2018.9 ± 54.3

whereas $\lambda_{SO}^I = 1$ for all targets. Thus we have only three parameters for all five targets.

In order to test the applicability of our approach to other observables, we have recently [27] analyzed the proton and neutron elastic-scattering, analyzing-power, total, and reaction cross-section data at 65 MeV from ^{12}C to ^{208}Pb. The agreement with the data is satisfactory. Here, we present our results (Table I) for only the total proton reaction cross section from even isotopes of tin and ^{208}Pb at 22.8 and 65.5 MeV. It is satisfying to note that the predictions of our model for almost all targets are within experimental uncertainties of the measurements of Refs. [38,39]. Furthermore, to compare our predictions over a wider energy region, we have also calculated reaction cross sections for p-^{118}Sn up to 220 MeV. Figure 6

shows that we get satisfactory agreement using relativistic kinematics with the data [38,40] up to 220 MeV. For the low-energy region ($10 \leqslant E < 65.5$ MeV), we find that the predictions of our model (i.e., all λ parameters set to unity) are in good agreement with the data, whereas for energies $65.5 \leqslant E < 220$ MeV, we have used the same normalizations ($\lambda_R = 0.722$, $\lambda_I = 0.760$, $\lambda_{SO}^R = 0.831$, and $\lambda_{SO}^I = 1.0$) as for Figs. 4 and 5.

In order to see the effect of relativistic kinematics, we compare our results with those obtained by using nonrelativistic kinematics. Although we do not show figures, the calculated central potentials are slightly deeper whereas the effect on the spin-orbit potential is marginal with the use of relativistic kinematics. Thus, the normalizations obtained for p-^{120}Sn with the nonrelativistic potentials are different ($\lambda^R = 0.80$,
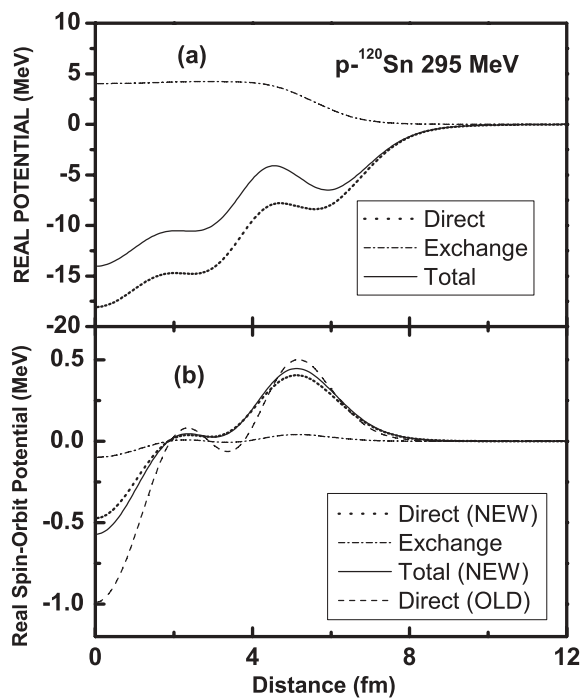

FIG. 3. Shows the calculated direct, exchange, and total (a) real central and (b) spin-orbit part of the calculated optical potential for p-^{120}Sn at 295 MeV. NEW denotes the results obtained using Eq. (1) whereas OLD denotes the use of BR approximation [26] (see text for details).
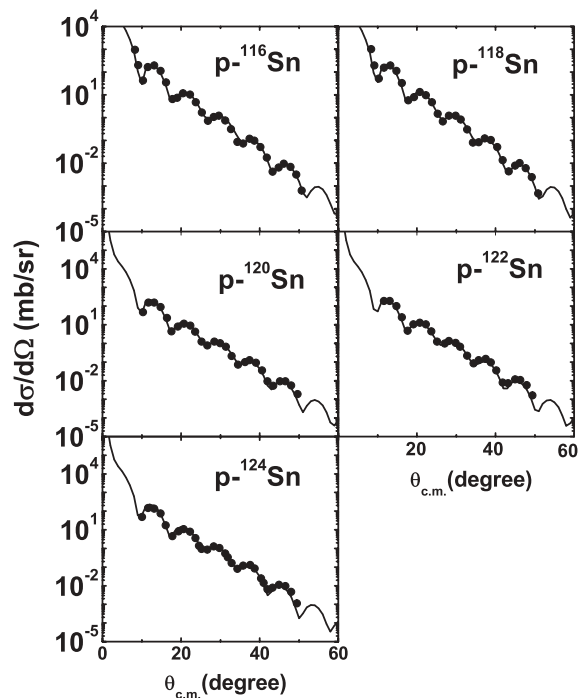

FIG. 4. Solid lines show the best fit obtained in the present work to the differential elastic cross-section data for the scattering of protons from tin isotopes. Sold circles are data from Ref. [14].
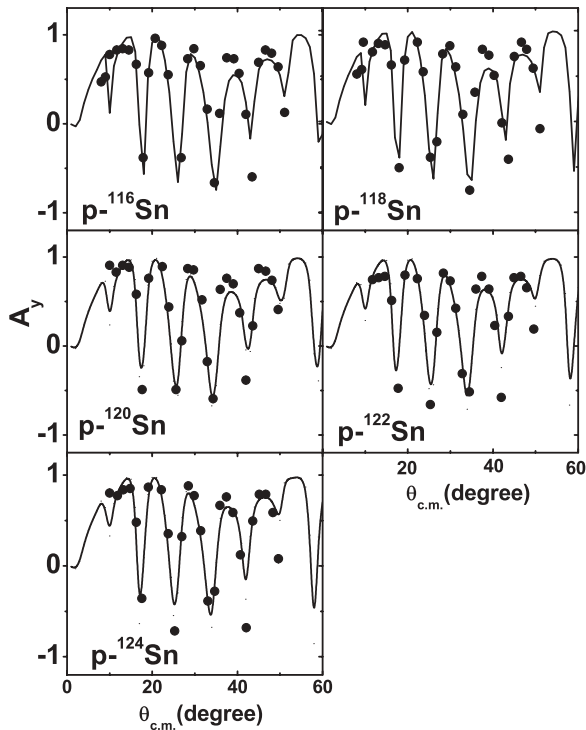
FIG. 5. Same as for Fig. 4 but for the analyzing-power data.

$\lambda^I = 0.9$, and $\lambda^R_{SO} = 0.8$). The results for other targets are similar.

Figure 7 shows our results for the differential cross section and the analyzing power due to the use of relativistic (solid curve) and nonrelativistic (dotted curve) kinematics in our model.

We see that the differential cross section shows noticeable changes only for angles greater than $55°$, whereas the analyzing-power data starts showing the effect of relativity for smaller angles ($>35°$) also. Note that there is negligible
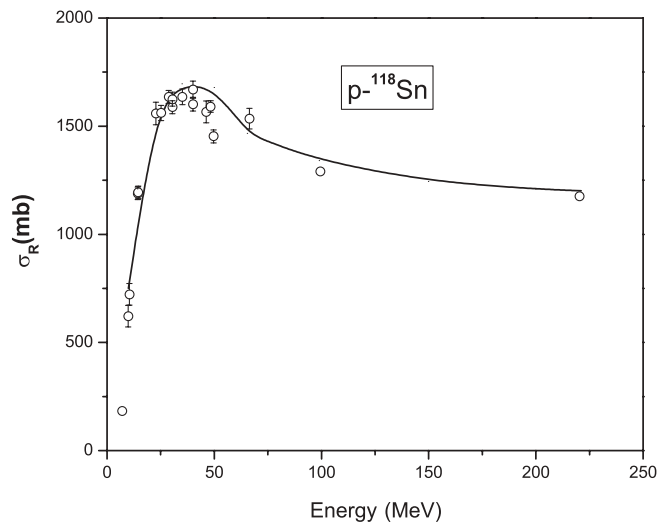

FIG. 6. Calculated reaction cross section for p-^{118}Sn. Solid line shows our result whereas open circles are the experimental data taken from Refs. [38,40].
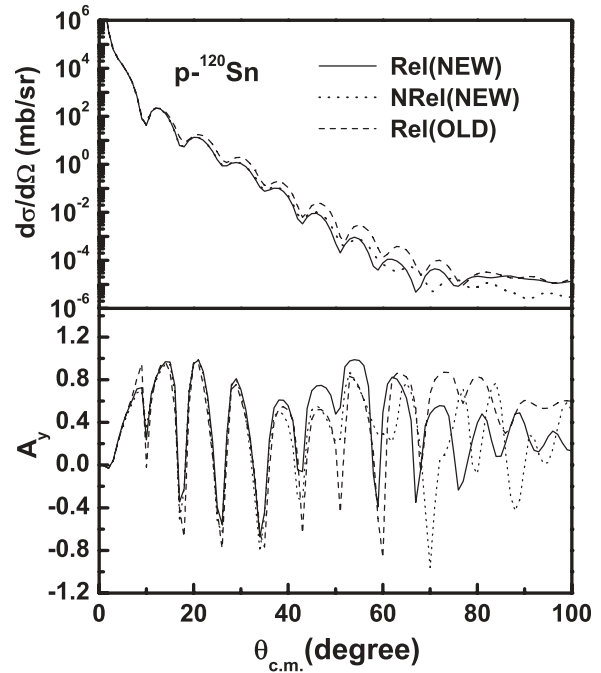

FIG. 7. Our predictions of the differential cross section and analyzing power for p-^{120}Sn at 295 MeV. Solid and dotted curves show the results due to relativistic (Rel) and nonrelativistic (NRel) kinematics. The dashed curve shows the effect of the BR approximation [26]. OLD and NEW symbols are same as for Fig. 3.

effect of relativistic kinematics for angles $<35°$. Because the proton-scattering data at this energy is available only up to $50°$, the analyzing-power data exhibits greater sensitivity to the relativistic kinematics. In view of the above, we conclude that the relativistic kinematic effects are non-negligible only for angles $>35°$ for proton scattering at 295 MeV.

In Fig. 7, we also show the effect on differential cross-section and analyzing-power data of using Eq. (1) instead of the BR approximation for calculating the spin orbit part of the potential. To see the effect of the spin-orbit potential, we keep the same central potential as used for Figs. 4 and 5. The solid line shows our results and the dashed line shows the results using the BR approximation for the direct part of the spin-orbit potential. We note that the use of the approximate spin-orbit potential overestimates the differential cross section at all angles except the extreme forward angles. Furthermore, the analyzing power predictions are also severely affected, especially for angles $\geqslant 40°$. A similar result with the use of Brueckner theory [8] was obtained for the proton scattering data from ^{40}Ca and ^{208}Pb in the 200- to 500-MeV region. Thus, we find that the proton differential cross-section data is quite sensitive, even at intermediate angles, to the spin-orbit potential at intermediate energies. Furthermore, because Eq. (1) can be easily evaluated, there is no need to use the approximation suggested by Brieva and Rook [26] for calculating the direct part of the spin-orbit potential.

In conclusion, we find that the relativistic kinematic effects are important at large angles whereas the spin-orbit potential influences the observables even at small angles.
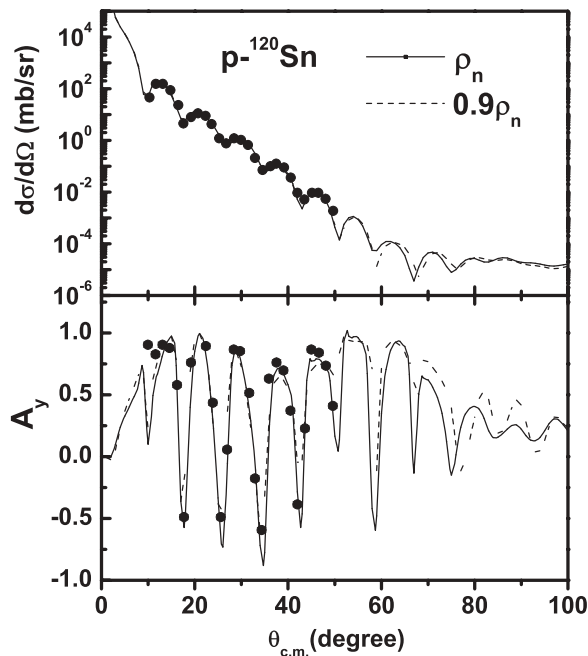
FIG. 8. Our results for the differential cross section and analyzing power for p-^{120}Sn. Solid curves are same as in Fig. 4, whereas dashed curves show our predictions after 10% reduction in neutron density ρ_n.

In order to see the sensitivity of our predictions on neutron distributions in the target, we have repeated our calculations with neutron densities reduced by 10%. This reduction of density would not change the rms radius of the neutron distribution. Our results are shown in Fig. 8.

We note that there are only minor changes in the differential cross section for angles $\geqslant 60°$, whereas non-negligible effects on analyzing power are present even at small angles. In view of

the results of Ref. [37], it seems that the present angular range and accuracy of the scattering data are consistent with a range of values for neutron-skin thicknesses. It is important to note that the experimental densities obtained at 800-MeV proton scattering from ^{58}Ni are consistent with a neutron skin [41,42] from -0.036 to -0.011 fm, whereas our RMF calculations give a value of 0.048 fm. Furthermore, Terashima *et al.* [14] have used zero neutron-skin thickness for ^{58}Ni. In addition, we note that the radial shape of the experimental densities in ^{58}Ni are substantially different from RMF results for distances <4.0 fm. (see also Fig. 4(a) of Ref. [15]). Our detailed results of the density dependence of proton scattering in the energy range 30 to 300 MeV from ^{58}Ni will be reported elsewhere.

IV. CONCLUSIONS

We obtain reasonably satisfactory agreement with the new 295-MeV proton scattering data [14] from tin isotopes using a nonrelativistic g-matrix approach with relativistic kinematics and an improved calculation of the spin-orbit potential. The RMF (RHB) nucleon density distributions used here yields a satisfactory description of tin isotopes and predicts a regular increase in the neutron skin with increasing neutron number. The skin thicknesses predicted by our RHB calculations are slightly larger than the RIA results in Ref. [14]. In conclusion, we find that the approach used here gives a satisfactory description of proton scattering from tin isotopes at 295 MeV.

[1] A. Nadasen, P. Schwandt, P. P. Singh, A. D. Bacher, P. T. Debevee, M. D. Kaichuck, and J. T. Meck, Phys. Rev. C **23**, 1023 (1981); P. Schwandt, H. O. Meyer, W. W. Jacobs, A. D. Bacher, S. E. Vigdor, M. D. Kaitchuck, and T. R. Donoghue, *ibid.* **26**, 55 (1982).

[2] S. Typel and B. A. Brown, Phys. Rev. C **64**, 027302 (2001).

[3] P. Danielewicz, Nucl. Phys. **A727**, 233 (2003).

[4] S. Karataglidis, K. Amos, B. A. Brown, and P. K. Deb, Phys. Rev. C **65**, 044306 (2002).

[5] K. Amos, S. Karataglidis, and J. Dobaczewski, Phys. Rev. C **70**, 024607 (2004).

[6] L. G. Arnold *et al.*, Phys. Rev. C **19**, 917 (1979); **25**, 936 (1982).

[7] A. M. Kobos, E. D. Coopper, J. I. Johansson, and H. S. Sherif, Nucl. Phys. **A445**, 605 (1985), and references therein.

[8] D. A. Hutcheon *et al.*, Nucl. Phys. **A483**, 429 (1988).

[9] H. V. von Geramb, in *Interaction Between Medium Energy Nucleons in Nuclei—1982, New York, NY*, Proceedings of Bloomington Conference, AIP Conf. Proc. No. 97, edited by H. O. Mayer (AIP, New York, 1982).

[10] K. Kaki and H. Toki, Nucl. Phys. **A696**, 453 (2001).

[11] D. P. Murdock and C. J. Horowitz, Phys. Rev. C **35**, 1442 (1987); C. J. Horowitz, *ibid.* **31**, 1340 (1985).

[12] N. Ottenstein, S. J. Wallace, and J. A. Tjon, Phys. Rev. C **38**, 2289 (1988).

[13] Y. Sugahara and H. Toki, Nucl. Phys. **A579**, 557 (1994); Y. Sugahara, Doctoral Thesis, Tokyo Metropolitian University, 1995.

[14] S. Terashima *et al.*, Phys. Rev. C **77**, 024317 (2008).

[15] H. Sakaguchi *et al.*, Phys. Rev. C **57**, 1749 (1998).

[16] G. E. Brown, A. Sethi, and N. M. Hintz, Phys. Rev. C **44**, 2653 (1991).

[17] Y. K. Gambhir, P. Ring, and A. Thimet, Ann. Phys. (NY) **198**, 132 (1990).

[18] P. Ring, Prog. Part. Nucl. Phys. **37**, 193 (1996), and references therein.

[19] Y. K. Gambhir, A. Bhagwat, and M. Gupta, Ann. Phys. (NY) **320**, 429 (2005), and references therein.

[20] G. A. Lalazissis, J. Konig, and P. Ring, Phys. Rev. C **55**, 540 (1997).

[21] J. F. Berger, M. Girod, and D. Gogny, Nucl. Phys. **A428**, 23 (1984).

[22] T. Gonzalez-Llarena *et al.*, Phys. Lett. B **379**, 13 (1996).

[23] W. Haider, A. M. Kobos, and J. R. Rook, Nucl. Phys. **A480**, 1 (1988); N. Yamaguchi, S. Nagata, and J. Matsuda, Prog. Theor. Phys. **70**, 459 (1983).

[24] S. M. Saliem and W. Haider, Phys. G: Nucl. Part. Phys. **28**, 1313 (2002).

[25] M. Hemalatha, Y. K. Gambhir, S. Kailas, and W. Haider, Phys. Rev. C **75**, 037602 (2007).

[26] F. A. Brieva and J. R. Rook, Nucl. Phys. **A297**, 206 (1978).

[27] W. Haider and M. Sharma, Int. J. Mod. Phys. E (IJMPE-S-09-00097) (to be published).

[28] L. E. Lagaris and V. R. Pandharipande, Nucl. Phys. **A359**, 331 (1981).

[29] M. Hemalatha, Y. K. Gambhir, W. Haider, and S. Kailas, Phys. Rev. C **79**, 057602 (2009).

[30] H. de Vries, C. W. de Jager, and C. de Vries, At. Data Nucl. Data Tables **36**, 495 (1987).

[31] C. Piller *et al.*, Phys. Rev. C **42**, 182 (1990).

[32] I. Angeli, At. Data Nucl. Data Tables **87**, 185 (2004).

[33] L. Ray, Phys. Rev. C **19**, 1855 (1979).

[34] A. Krasznahorkay *et al.*, Nucl. Phys. **A567**, 521 (1994).

[35] A. Krasznahorkay *et al.*, Phys. Rev. Lett. **82**, 3216 (1999).

[36] A. Trzcinska, J. Jastrzebski, P. Lubinski, F. J. Hartmann, R. Schmidt, T. von Egidy, and B. Klos, Phys. Rev. Lett. **87**, 082501 (2001).

[37] J. Piekarewicz and S. P. Weppner, Nucl. Phys. **A778**, 10 (2006).

[38] R. F. Carlson, At. Data Nucl. Data Tables **63**, 93 (1996).

[39] A. Auce, A. Ingemarsson, R. Johansson, M. Lantz, and G. Tibell, Phys. Rev. C **71**, 064606 (2005).

[40] A. V. Sannikov and E. N. Savitskaya, Radiation Protection Dosimetry **110**, 27 (2004).

[41] G. S. Blanpied *et al.*, Phys. Rev. Lett. **39**, 1447 (1977).

[42] L. Ray, W. Rory Coker, and G. W. Hoffmann, Phys. Rev. C **18**, 2641 (1978).